

A 46 μ W 13 b 6.4 MS/s SAR ADC With Background Mismatch and Offset Calibration

Ming Ding, Pieter Harpe, *Senior Member, IEEE*, Yao-Hong Liu, *Member, IEEE*,
Benjamin Busze, Kathleen Philips, and Harmke de Groot, *Member, IEEE*

Abstract—A 6.4 MS/s 13 b ADC with a low-power background calibration for DAC mismatch and comparator offset errors is presented. Redundancy deals with DAC settling and facilitates calibration. A two-mode comparator and 0.3 fF capacitors reduce power and area. The background calibration can directly detect the sign of the dynamic comparator offset error and the DAC mismatch errors and correct both of them simultaneously in a stepwise feedback loop. The calibration achieves 20 dB spur reduction with little area and power overhead. The chip is implemented in 40 nm CMOS and consumes 46 μ W from a 1 V supply, and achieves 64.1 dB SNDR and a FoM of 5.5 fJ/conversion-step at Nyquist.

Index Terms—Background calibration, comparator offset, DAC mismatch, low power, redundancy, SAR ADC.

I. INTRODUCTION

WIRELESS standards, e.g., 802.15.4g, need high resolution ADCs (>10 b) and MS/s sampling rates with very low power to tackle with large interferences during communication. The SAR ADC is well known for its excellent power efficiency. However, there are several challenges when the resolution goes beyond 10 b: first, the intrinsic DAC matching is practically limited up to 10–12 b in modern CMOS technologies [1]. Scaling up the device dimensions can improve matching but it will deteriorate power-efficiency and speed. Alternatively, calibrations [2]–[6] are introduced to correct the errors and push the SNDR beyond 62 dB. Reference [2] uses an off-chip DSP engine to correct the ADC errors through a least-mean-square (LMS) algorithm in the background, but the overhead in area and power is high. Reference [3] uses a similar idea with less overhead, but it cannot run in the background without interrupting the normal ADC operation. References [4] and [5] rely on a statistics-based method to calibrate the capacitor errors in the foreground. However, the statistics-based methods usually have significant overhead in latency, area, and power and are thus implemented off-chip.

Besides DAC mismatch, noise tends to limit the performance of high-resolution SAR ADCs in modern CMOS,

especially with reduced supply voltage (≤ 1 V). To achieve the required noise level while still saving power, several techniques have been proposed. A two-stage pipelined SAR ADC [6]–[10] can relax the comparator noise by introducing a low-noise amplifier between the two stages. Nonetheless, the effort to design a low-power amplifier and to overcome the induced errors (e.g., gain error and offset error) is not trivial. References [11] and [12] relax the comparator noise by oversampling the comparator, but they sacrifice speed due to the additional cycles. Alternatively, the comparator can be made as reconfigurable to save power while still maintaining precision [13], [14]. However, this also introduces a dynamic comparator offset, which may impede the overall accuracy of the ADC.

To counteract the issues mentioned earlier, this design successfully implements a 13 b SAR ADC with a reconfigurable comparator and low-power on-chip background calibration for both the DAC mismatch errors and dynamic comparator offset [15]. The background calibration utilizes a redundancy facilitated error-detection scheme and an analog correction scheme, which will be discussed later. Thanks to the low-power calibration, this ADC achieves an ENOB of 10.4 b and a state-of-the-art power-efficiency of 5.5 fJ/conversion-step at 6.4 MS/s.

Section II introduces the SAR ADC architecture as well as the principle of the calibration. In Section III, the implementation of the SAR ADC is shown. The measurement results are presented in Section IV, and conclusions are given in Section V.

II. SAR ARCHITECTURE AND SIGN-BASED CALIBRATION

Calibration offers the possibility to save substantial power in the DAC and comparator by calibrating their errors. However, the calibration overhead in area, speed, power, as well as architecture complexity should be kept to a minimum. Foreground calibration can compensate the error at one time, but it usually needs special analog input signals (e.g., shorting input [5]) or doubled operating clock [3]. This becomes more cumbersome when more errors need to be calibrated. Besides, foreground calibration is not able to track the time-varying errors (e.g., offset) due to environmental changes. To do that, the foreground calibration has to be repeated periodically. This is neither convenient nor efficient for a radio system. Instead, background calibration can run in the background and still calibrate the errors without interrupting the normal ADC operation.

Manuscript received June 9, 2016; revised August 19, 2016; accepted September 7, 2016. Date of publication October 19, 2016; date of current version January 30, 2017. This paper was approved by Associate Editor Ichiro Fujimori.

M. Ding, Y.-H. Liu, B. Busze, K. Philips, and H. de Groot are with imec-nl, Holst Centre, 5605 Eindhoven, The Netherlands (e-mail: ming.ding@imec-nl.nl).

P. Harpe is with the Eindhoven University of Technology, 5612 AZ Eindhoven, The Netherlands.

Color versions of one or more of the figures in this paper are available online at <http://ieeexplore.ieee.org>.

Digital Object Identifier 10.1109/JSSC.2016.2609849

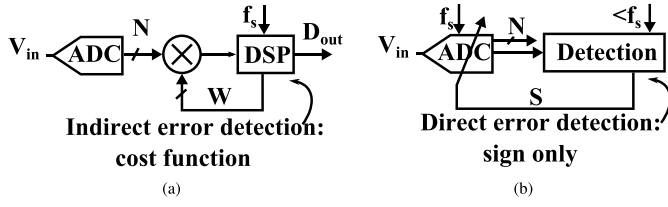


Fig. 1. (a) Block diagram of the prior arts' calibration method and (b) proposed calibration method for a N bit ADC.

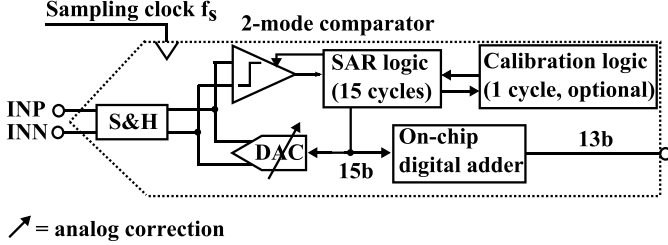


Fig. 2. Block diagram of a 13 b SAR ADC.

In prior art, without knowing any information of the error, often the circuit errors are corrected indirectly in a digital fashion [2], [3], [10] via postprocessing. Fig. 1(a) shows the block diagram of the calibration method in [2], [3], and [10]. Based on the ADC output data, a DSP engine can define a cost function, which reflects the error. Through an adaptive algorithm, e.g., LMS, the value of the cost function will be tuned toward zero once the coefficients W are correctly trained. To guarantee the precision of the coefficient training, redundancy is usually introduced in the DSP engine. On the other hand, a direct error detection and correction scheme is proposed as shown in Fig. 1(b). The sign of error can be detected as shown later. Thanks to the feedback loop and the analog correction circuit, it is very convenient to stepwise tune the error toward zero based on its sign. In this way, only the sign needs to be processed compared with the whole ADC output in Fig. 1(a). Besides, power-hungry operations [e.g., multiplying in Fig. 1(a)] are avoided and only much simpler calculations (e.g., accumulation) are needed. Furthermore, instead of a blind algorithm requiring many iterations, the sign of the individual errors can be directly detected to compensate these errors, reducing the convergence time and required energy. Moreover, the actual correction is in analog domain instead of digital signal processing as shown later, consuming far less power. Overall, the proposed calibration method has very little overhead in circuit complexity, area, speed, and power.

A. ADC Architecture

Fig. 2 shows the architecture of the 13 b SAR ADC. In each SAR conversion, first, the S&H samples the differential analog input voltage on the capacitor arrays inside the DAC. Using the comparator and the logic, the DAC output will approximate the sampled input voltage in several comparisons through a successive-approximation algorithm using a monotonic switching scheme [16]. In this design, a total of 15 cycles is used to perform a 13 b conversion, where two of them are redundant cycles to overcome various errors during the conversion (e.g., DAC settling and noise), similar to [14].

The 13 b output is calculated from the 15 b raw code by an on-chip digital adder. A two-mode comparator is introduced to save power while still maintaining accuracy. Optionally, an additional (16th) cycle can be activated for DAC mismatch calibration or comparator offset calibration as shown later. All the operations including the calibrations are asynchronously controlled. Thus, only one relatively low-frequency sampling clock f_s is needed for both normal operation and calibration.

Fig. 3 shows the conversion scheme as well as the DAC of the 13 b ADC. The 15 cycles include ten coarse cycles and five fine cycles, where the 7th and 11th cycle are the redundant cycles. The first redundant bit (7th cycle) relaxes DAC settling time and facilitates the DAC mismatch calibration, which will be explained later. Considering that the worst mismatch errors happen for the largest capacitors, only the first five DAC capacitors are calibrated in this paper. The capacitors lower than the redundant bit are not calibrated; thus, they need to be sufficiently linear intrinsically. Thanks to the second redundant bit (11th cycle), a two-mode comparator can be employed [14]. This redundancy allows, first of all, the decision errors during the coarse comparisons due to the comparator noise, thus allowing a low-power mode comparator. Furthermore, since the redundancy can tolerate the residual comparator offset error after calibration as shown later, the comparator offset calibration accuracy can be relaxed. The combination of postcalibration comparator offset and coarse comparator noise should remain within the redundancy range of the 11th bit, which can tolerate errors up to $\pm 8\text{LSB}$.

B. Comparator Offset Error Detection

As mentioned earlier, the comparator works in the low-power mode for the first cycles (coarse cycles), and it only switches to the low-noise mode with higher power for the last few cycles (fine cycles). In this way, the overall power consumption of the comparator is reduced while it still satisfies the noise requirement of the ADC. However, the two-mode comparator will have two different offsets for the corresponding two modes. Once this dynamic offset is beyond the redundancy range ($\pm 8\text{LSB}$), the ADC performance cannot be recovered. Therefore, calibration of the dynamic offset becomes necessary. The goal of the comparator offset calibration is to minimize the offset difference V_{Δ} , which equals $V_{\text{off}1} - V_{\text{off}2}$. Since a feedback loop [Fig. 1(b)] is used to minimize V_{Δ} stepwise, rather than post processing, it is sufficient to detect the sign of V_{Δ} only in order to minimize its value.

The comparator dynamic offset detection is shown in Fig. 4. The equivalent voltage at the comparator input V_{eq} can be viewed as a summation of the sampled input signal V_{in} , DAC reference voltage (V_{DAC}), and the input-referred comparator offset [$V_{\text{off}1(2)}$]. The optional additional (16th) cycle is performed on top of the 15-cycle comparison for a 13 b ADC. The same comparison as the last (15th) cycle is repeated in the additional (16th) cycle. The DAC code remains unchanged, but the comparator switches from *mode2* to *mode1*. Ideally, if the two offsets are the same, the comparison result of the last cycle (D_{15}) and the additional cycle (D_{16}) would be the same. However, if the offsets are different, then the equivalent

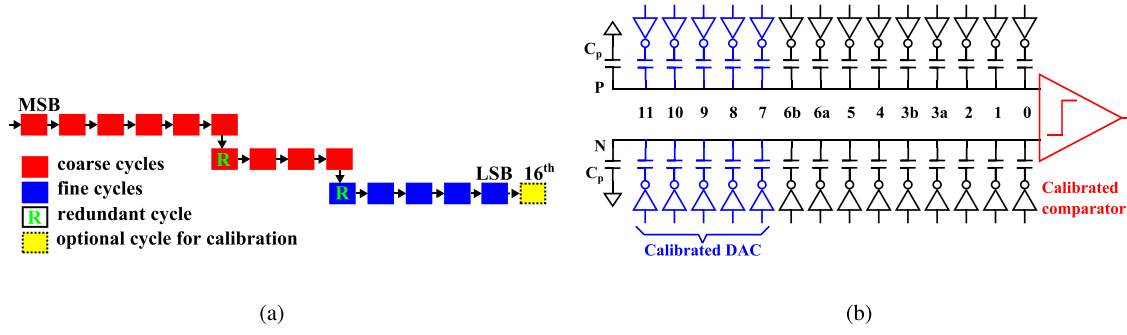


Fig. 3. (a) Conversion scheme and (b) DAC of the 13 b SAR ADC.

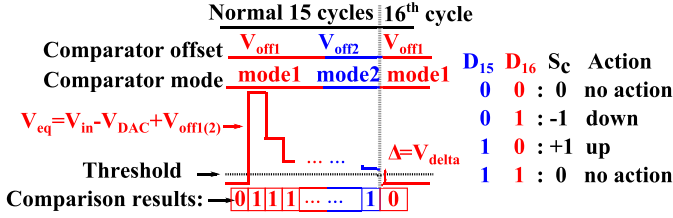


Fig. 4. Illustration of the principle for the comparator dynamic offset detection.

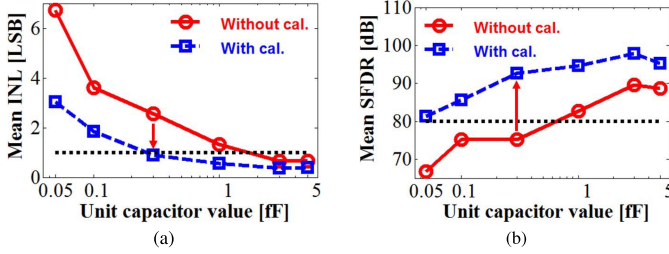


Fig. 5. Unit capacitor value and its impact on the 13 b ADC performance. (a) Mean INL and (b) mean SFDR in ten runs.

analog voltage (V_{eq}) would be different, thus causing different comparison results. The difference of D_{15} and D_{16} reveals the sign of the offset difference S_c and thus the direction in which the comparator correction circuit needs to be tuned.

C. DAC Mismatch Calibration

The unit capacitor C_u in an SAR DAC is mainly sized for two considerations: kT/C noise and capacitor mismatch error [17], [18]. When the ADC resolution goes beyond 10 b, C_u tends to be limited by the capacitor mismatch and thus has to be sized significantly large, degrading power efficiency. Alternatively, C_u can be sized to just meet the kT/C noise to save power, and use calibration to compensate the capacitor mismatch error. To investigate the relation between the unit capacitor size and the ADC performance, a Monte-Carlo simulation in MATLAB is performed. Fig. 5(a) and (b) shows the simulated mean value of the worst case INL and SFDR of the 13 b ADC against the unit capacitor value with and without the proposed DAC capacitor calibration in ten runs. For simplification, only capacitor mismatch errors are considered. In this design, to reach an acceptable INL error of ≤ 1 LSB, C_u has to be as large as 3 fF without calibration. As can be seen, with calibration, the unit capacitor value can

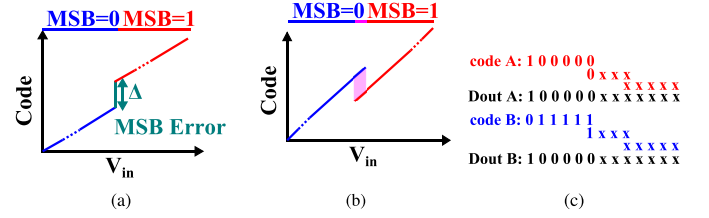


Fig. 6. (a) Illustration of an ADC transfer characteristic with MSB capacitor mismatch. (b) and (c) Illustration of redundancy inside an ADC.

be reduced to only 0.3 fF while maintaining $INL < 1$ LSB and $SFDR > 90$ dB. In this way, calibration saves ten \times switching power, while also reducing chip area and increasing conversion speed. Please note that only the first five capacitors are calibrated. The lower capacitors are not calibrated and are thus limiting the ADC performance after calibration.

For DAC capacitor mismatch calibration, the principle is based on the detection of DNL errors, which indicates capacitor mismatch. Fig. 6(a) shows an example of an ADC with an exaggerated DNL error Δ at the MSB capacitor. A similar picture could be drawn for the other bits of the DAC. Thanks to the redundancy, there is a convenient way to detect the sign of Δ , which is sufficient for the feedback loop in the ADC [Fig. 1(b)] to tune Δ toward zero. As shown in Fig. 6, the redundancy (i.e., 15 raw bits for a final 13 bits) implies that there are multiple 15 b codes describing the same final 13 b output. For instance, codes A and B [Fig. 6(c)] will resolve the same 13 b output code and are thus equivalent. However, the bits inside code A and B are different, and hence the activated capacitors to generate these two codes are also different.

V_A and V_B represent the DAC voltage of the codes A and B. If there is no capacitor mismatch, the sum of the activated capacitors in code A and B is equal, and V_A and V_B are equal. On the other hand, if there is capacitor mismatch, the sum of the activated capacitors is not identical for the codes A and B, and thus V_A and V_B will not be the same. This can be used as follows to perform a calibration as shown in Fig. 7(a): if code A is observed during a normal 15-cycle SAR conversion, a 16th cycle is added, and an additional comparison is performed. Before the 16th cycle takes place, the internal code is updated to code B. On the other hand, if code B is detected, the internal code will switch to code A. In this way, the comparator result of the 16th cycle (D_{15}) in comparison with the result in the 16th cycle (D_{16}) will

TABLE I
CODE PATTERNS FOR CALIBRATION ACTIVATION

Calibration of:	Code		
	MSB		LSB
	XXXXXXX	YYY	ZZZZZ
MSB	0111111/1000000	110	XXXXXX
MSB-1	0011111/0100000	110	XXXXXX
MSB-2	0101111/0110000	110	XXXXXX
MSB-3	0110111/0111000	110	XXXXXX
MSB-4	0111011/0111100	110	XXXXXX
Comparator	11000XX	110	XXXXXX

save power. The *Sense&Force* circuit will constantly monitor the internal DAC code. As mentioned earlier, certain DAC codes trigger the calibration. If one of these calibration codes occurs during the 15 comparisons, *Sense&Force* will activate the calibration by enabling the 16th cycle. Before the 16th comparison, either the DAC or the comparator needs to be switched as mentioned earlier for calibration. If the DAC calibration is detected, the *Sense&Force* will force the DAC code to its alternative (e.g., 1000000x to 0111111x) through the multiplexer. Similarly, if the comparator calibration is detected, the *mode set* block will switch the comparator from *mode2* to *mode1*. After that, the comparison of the 16th cycle will be performed. Once the 16th comparison is completed, the *calibration algorithm* block will determine the sign of the error (S_c or S_{dac}) based on the comparison results of the last two cycles (D_{15} and D_{16}). The sign of the error will first be processed by a digital low-pass filter (LPF) to filter out noise and then accumulated in the block *Cal. register* for the analog correction circuits.

A. Calibration Logic Implementation

Although the DAC calibration could be performed as a start-up foreground calibration, since the capacitor values are relatively stable against environment variations, in this paper, it is still put in the background for two reasons. First, it avoids dedicated time at start-up for calibration. Second, thanks to the low-power implementation, the penalty by performing it in the background is negligible. The proposed calibration methods can work continuously in the background to track the time-varying errors due to environmental changes. Thus, the power consumption of the calibration circuit should be kept low to reduce the power consumption overhead. To reduce power, two methods have been used. First of all, to avoid unnecessary switching in the digital circuit, the specific codes that enable calibration are carefully chosen to limit the activation rate of the calibration. Table I shows the code pattern for the comparator calibration and the five capacitors in the DAC. For clarification, the 15-bit internal DAC code is divided into a 7 b X-code, a 3 b Y-code, and a 5 b Z-code. For the DAC calibration, the first 7 b X-code is needed for detection as mentioned earlier. For the comparator offset calibration, it is arbitrarily set to 11000xx, since it can be any code. Therefore, the total activation rate of both calibrations would be about 10.9% ($((10 + 4)/2^7)$). Moreover, the Y code is set to code 110 to further reduce the activation rate down to 1.4% ($(10.9\%/2^3)$). Overall, the detection codes are set around the

center of the code range (2–6 k out of the 0–8 k range), to ensure calibration even when the input is below full scale.

As a second step to save power, the calibration logic is custom designed. Section III-A1 describes several critical blocks in the calibration path, which are the *Sense&Force*, the LPF, and the calibration register implementation.

1) *Dynamic Logic for Code Detection*: The *Sense&Force* circuit is continuously monitoring the internal DAC code, which changes in each conversion. The traditional CMOS logic (e.g., inverter) switches when the input signals toggle. If implemented in standard CMOS logic, the detection circuit may still consume power even if the internal DAC code is irrelevant for calibration. In the example shown in Fig. 11(a), the circuit is used to detect the X-code 0111111. However, at any other X-code, which is not desired for calibration, although the output stays unchanged, the internal logic gates in the circuits are still switching, increasing power consumption. To reduce this unnecessary switching activities, dynamic logic is introduced to implement the *Sense* circuit as shown in Fig. 11(b). In each conversion, the output node A of each single slice in the detection logic is reset to low. Only when the specific code pattern is observed in the DAC, node A of the dynamic logic will be charged to high. In the example slice shown, DAC calibration of the MSB is activated by $DAC_U < 4 >$ if the X-code equals 0111111, Y-code equals 110, and DAC calibration is active ($EN_D = 1$). The other ten slices works in a similar way using the codes in Table I. The 16th cycle is enabled when one of the calibrations is activated. Considering that for the 11 slices only 14 out of the 128 X-codes can activate the circuit, most of the time ($\sim 90\%$) the circuits are inactive. In this way, the switching frequency, thus the power consumption of the detection circuit, is significantly reduced.

2) *Low-Pass Filter*: After the sign of the error (S_c and S_{dac} in Fig. 10) is determined, it will be processed by a LPF to filter out the noise. Fig. 12(a) shows the schematic of the implemented LPF. In total, six filters are implemented: five for the DAC calibration and one for the comparator calibration. Each slice is implemented with a 6 b bidirectional counter. The unit element of the counter, one D flip-flop and three logic gates, can perform both up counting and down counting. Two signals INC_I and DEC_I represents the polarity of the sign: up or down. In the example shown in Fig. 12(b), the counter is counting up when the signal INC_I is valid. If accidentally the signal DEC_I becomes high (e.g., due to noise), the counter will temporally count down. Once INC_I becomes valid again, the counter will count up to 63 and generate a short pulse for the signal INC_O . Similarly, a short pulse can be generated for DEC_O when the counter is counted down to 0. In such a way, the decision errors during the calibration due to random noise can be filtered out. After that, INC_O (or DEC_O) will increment (decrement) the actual calibration register value. During normal operation when calibration is not active, both the signals INC_I and DEC_I are low. In this case, the counter will stop counting while still maintaining the counted number. Therefore, the power consumption of the circuit is kept to a minimum when no calibration happens.

TABLE II
CAPACITOR VALUES IN (a) THE MAIN DAC AND (b) CALIBRATION DAC

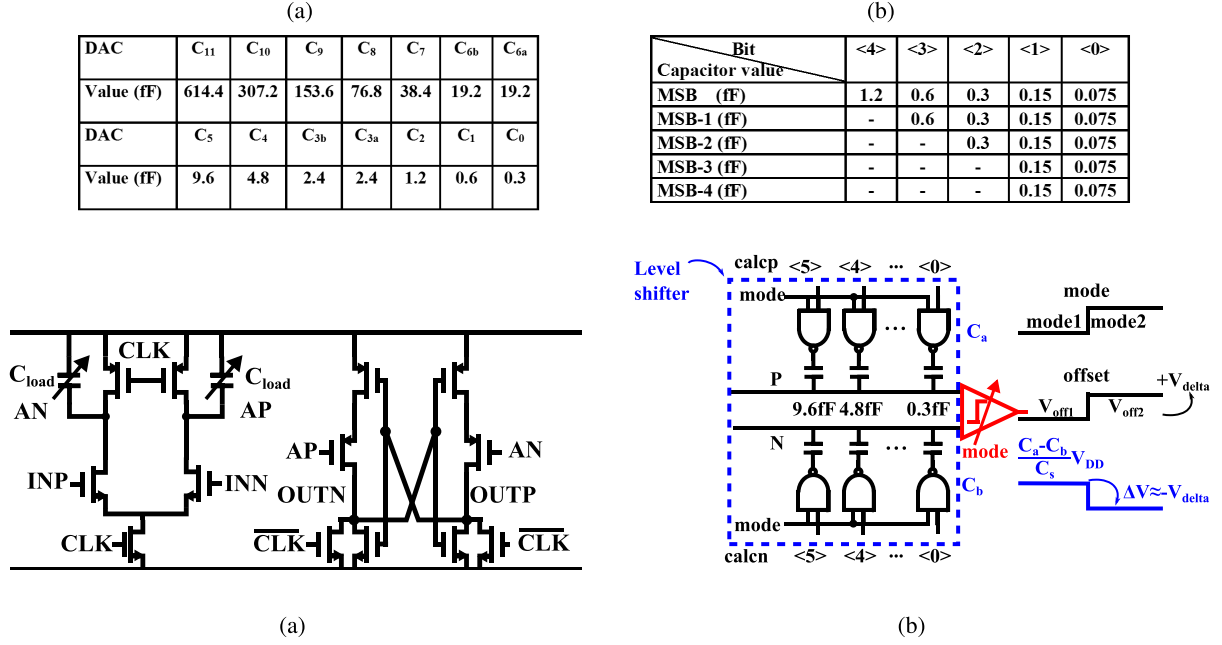


Fig. 14. (a) Comparator schematic and (b) correction circuits of comparator dynamic offset.

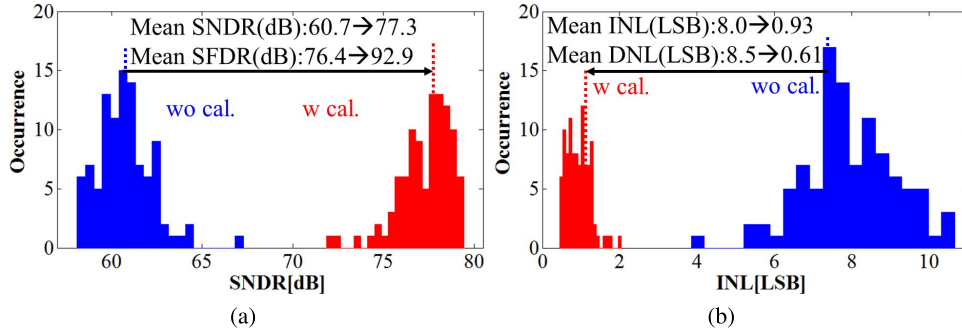


Fig. 15. Simulated performance of the ADC with/without implemented calibrations (100 runs): (a) SNDR and (b) INL.

the comparator to 0.3 mV with 337 fJ energy consumption. In this way, the total energy consumption of the comparator is reduced from 5055 to 2565 fJ, saving two times comparator power while still maintaining the same accuracy. Furthermore, a programmable array of C_{load} capacitors could be used for comparator offset correction [5]. However, this type of offset correction would also impact comparator power, speed, and noise. Therefore, to avoid these side effects, the offset difference in the two modes is corrected by two programmable capacitors (C_a and C_b) that switch when the comparator changes mode, thus inducing a voltage step $V_P - V_N$, which equals to $(C_a - C_b)/(C_s)V_{DD}$. This voltage step counteracts the offset step once the calibration is correctly settled. As shown in Fig. 14(b), C_a and C_b use a binary-scaled bank of capacitors and allow an offset correction of up to ± 63 LSB with 1LSB steps. Note that the remaining offset error after calibration (within 1LSB) is inherently compensated by the redundancy.

Thanks to the simple calibration algorithm and the custom-designed dynamic logic, the active area of the digital calibration circuit is only 0.0017 mm² while the analog correction circuit is about 0.0009 mm². To prove the concept of calibration, simulations in MATLAB are executed with kT/C noise, comparator dynamic offset and DAC mismatch considered. Fig. 15 shows the Monte Carlo simulation results (100 runs) of the ADC before and after calibration. The input signal is set to a sinewave. It is clear that calibration can correct the errors due to the device imperfections and improve the ADC performance significantly.

IV. MEASUREMENTS

The SAR ADC is implemented in 40 nm CMOS technology (Fig. 16) and occupies 0.0675 mm². With calibration enabled, the ADC consumes 46 μ W from a 1 V supply voltage at 6.4 MS/s. Fig. 17 shows the power break down of the ADC based on both the measured and simulated values. It can

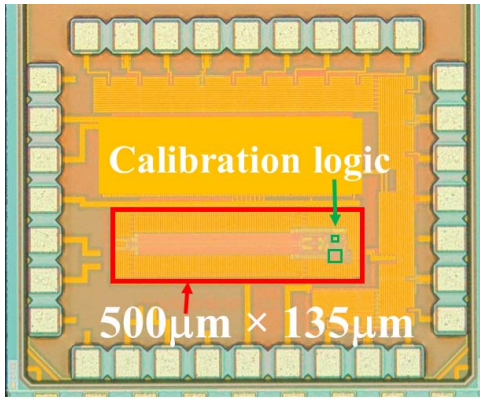


Fig. 16. Die photo in 40 nm CMOS.

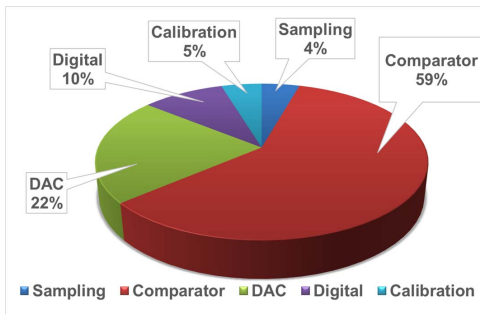


Fig. 17. Power consumption breakdown of the chip.

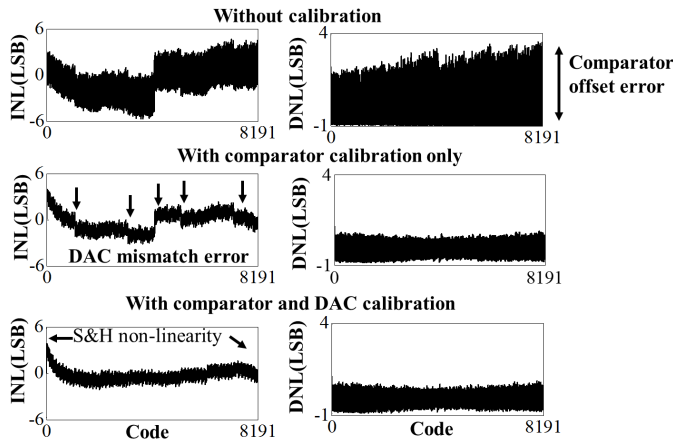


Fig. 18. Measured INL/DNL of the chip in three scenarios: without calibration, with comparator offset calibration, and with both calibrations.

be seen that the calibration power is almost negligible (5%). Figs. 18 and 19 show the INL/DNL and the spectrum in three scenarios: without calibration, with comparator calibration only, and with both the comparator and DAC calibrations. The large initial DNL errors, caused by dynamic comparator offset, are effectively reduced when comparator calibration is enabled. The DAC calibration suppresses the INL errors due to DAC mismatch, as shown in Fig. 18. The final INL is limited by sampling switch distortion. Still, the spurs due to comparator offset and DAC mismatch are suppressed by 20 dB (Fig. 19). Therefore, the SNDR and SFDR are

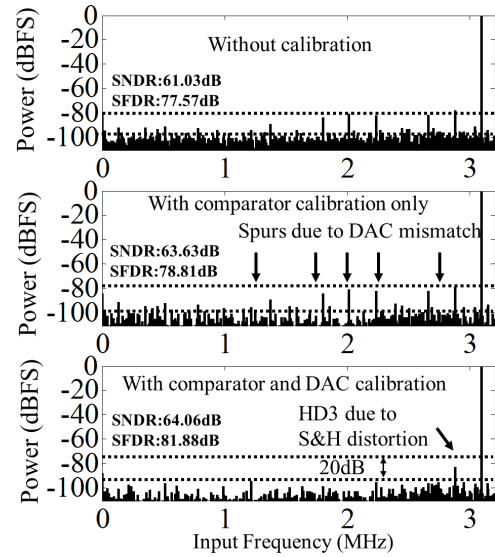


Fig. 19. Measured spectrum of the chip in three scenarios: without calibration, with comparator offset calibration, and with both calibrations.

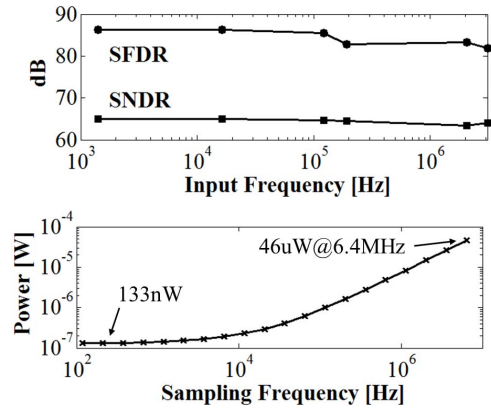


Fig. 20. Measured dynamic performance of the chip.

enhanced to 64.1 and 81.9 dB at Nyquist, respectively, achieving a 5.5 fJ/conv.step FoM. The SNDR is mainly noise limited by the total ADC noise (1.5LSB), which compromises for low power. Fig. 20 shows the dynamic performance with calibration enabled and the scaling of the power consumption (133 nW leakage level) with sampling rate. Fig. 21 shows the performance of four measured samples before and after calibration. Regardless of the magnitude of the errors, the calibration is capable to suppress the errors and improve the ADC performance. The convergence time of the calibration can be measured in the following way: The ADC data are captured with the calibrations first disabled, and then enabled. By using a moving window over the time for the sampled ADC data, and performing fast Fourier transforms for the data of each window, a figure of SNDR against time can be plotted as shown in Fig. 22. It takes approximately 400 k cycles for the ADC performance to settle. The measurement results are summarized and compared with the state-of-the-art in Table III. The power efficiency of this ADC is in line with the state-of-the-art, while also integrating an on-chip

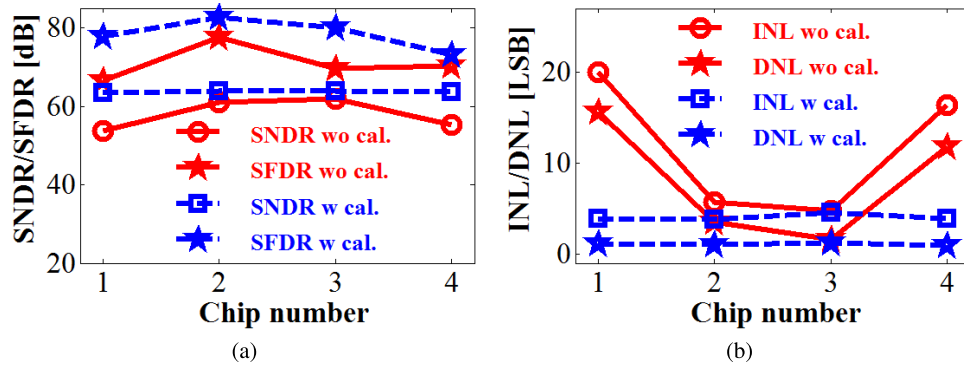


Fig. 21. Measured performance of four samples: (a) SNDR/SFDR and (b) INL/DNL.

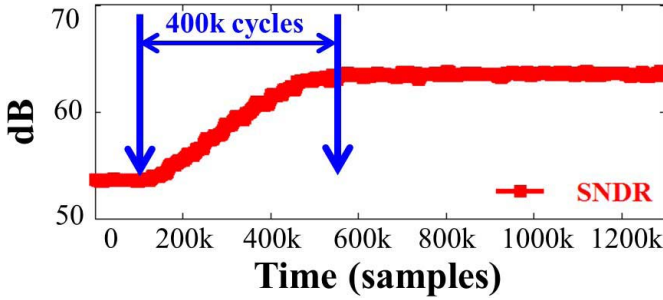


Fig. 22. Measured convergence time of the calibration loop.

TABLE III
PERFORMANCE COMPARISON OF THE ADC

	[2]	[3]		[6]	[12]	This work
Architecture	Algorithm mic	SAR		Pipelined SAR TI	SAR	SAR
Technology (nm)	250	130		28	65	40
Area (mm ²)	1.6	0.059		0.1369	0.076	0.0675
Resolution (bit)	16	12		14	12	13
Supply voltage (V)	2.5	1.2		1.0	0.6	1.0
Reference Voltage (V)	2.5	1.2		1.8	0.6	1.0
Sample rate (MS/s)	1	22.5	45	80	0.04	6.4
Power (uW)	105000	2790	2820	1500	0.097	46
INL (LSB)	4.8	-	-	-	1.9	3.79
DNL (LSB)	0.66	-	-	-	0.97	1.08
Nyquist SNDR (dB)	89**	70.1	67.1	66	62.5	64.1
Nyquist SFDR (dB)	-	90.3	84.7	74	68.8	81.9
FOMW_Nyquist (fJ/conv.step)	4560**	50.8	36.3	11.5	2.2	5.5
Calibration	Off-chip	Off-chip		On-chip	-	On-chip
Cal. Circuit Area (mm ²)	Not included	0.01*		Included	-	0.0026
Cal. Circuit Power(uW)	Not included	200*		Included	-	Included

*Estimated

**Based on SNR

background calibration technique for comparator offset and DAC mismatch.

V. CONCLUSION

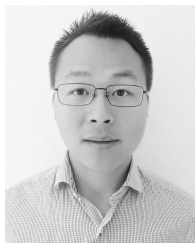
This paper demonstrated an SAR ADC with an on-chip background calibration. The calibration circuit can directly

detect the sign of the errors and apply feedback to the analog correction circuits, correcting both the comparator dynamic offset error and the DAC mismatch error at the same time. Thanks to the simple calibration algorithm and the custom-designed dynamic logic, the ADC achieves 5.5 fJ/conv.step at 6.4 MS/s with negligible overhead in area and power.

REFERENCES

- [1] C.-Y. Liou and C.-C. Hsieh, "A 2.4-to-5.2 fJ/conversion-step 10b 0.5-to-4 MS/s SAR ADC with charge-average switching DAC in 90 nm CMOS," in *IEEE ISSCC Dig. Tech. Papers*, Feb. 2013, pp. 280–281.
- [2] J. McNeill, M. C. W. Coln, and B. J. Larivee, "Split ADC architecture for deterministic digital background calibration of a 16-bit 1-MS/s ADC," *IEEE J. Solid-State Circuits*, vol. 40, no. 12, pp. 2437–2445, Dec. 2005.
- [3] W. Liu, P. Huang, and Y. Chiu, "A 12b 22.5/45 MS/s 3.0 mW 0.059 mm² CMOS SAR ADC achieving over 90 dB SFDR," in *IEEE ISSCC Dig. Tech. Papers*, Feb. 2010, pp. 380–381.
- [4] C. C. Lee, C.-Y. Lu, R. Narayanaswamy, and J. B. Rizk, "A 12b 70 MS/s SAR ADC with digital startup calibration in 14 nm CMOS," in *Proc. IEEE Symp. VLSI Circuits*, Jun. 2015, pp. C62–C63.
- [5] B. Verbruggen, M. Iriguchi, and J. Craninckx, "A 1.7 mW 11b 250 MS/s 2-times interleaved fully dynamic pipelined SAR ADC in 40 nm digital CMOS," *IEEE J. Solid-State Circuits*, vol. 47, no. 12, pp. 2880–2887, Dec. 2012.
- [6] F. van der Goes *et al.*, "A 1.5 mW 68 dB SNDR 80 MS/s 2 \times interleaved SAR-assisted pipelined ADC in 28 nm CMOS," *IEEE J. Solid-State Circuits*, vol. 49, no. 12, pp. 2835–2845, Dec. 2014.
- [7] B. Verbruggen, K. Deguchi, B. Malki, and J. Craninckx, "A 70 dB SNDR 200 MS/s 2.3 mW dynamic pipelined SAR ADC in 28 nm digital CMOS," in *IEEE Symp. VLSI Circuits Dig. Tech. Papers*, Jun. 2014, pp. 1–2.
- [8] Y. Zhou, B. Xu, and Y. Chiu, "A 12 bit 160 MS/s two-step SAR ADC with background bit-weight calibration using a time-domain proximity detector," *IEEE J. Solid-State Circuits*, vol. 50, no. 4, pp. 920–931, Apr. 2015.
- [9] Y. Lim and M. P. Flynn, "A 1 mW 71.5 dB SNDR 50 MS/s 13 bit fully differential ring amplifier based SAR-assisted pipeline ADC," *IEEE J. Solid-State Circuits*, vol. 50, no. 12, pp. 2901–2911, Dec. 2015.
- [10] R. Sehgal, F. van der Goes, and K. Bult, "A 12 b 53 mW 195 MS/s pipeline ADC with 82 dB SFDR using split-ADC calibration," *IEEE J. Solid-State Circuits*, vol. 50, no. 7, pp. 1592–1603, Jul. 2015.
- [11] T. Miki *et al.*, "A 4.2 mW 50 MS/s 13 bit CMOS SAR ADC with SNR and SFDR enhancement techniques," *IEEE J. Solid-State Circuits*, vol. 50, no. 6, pp. 1372–1381, Jun. 2015.
- [12] P. Harpe, E. Cantatore, and A. van Roermund, "A 2.2/2.7 fJ/conversion-step 10/12b 40 kS/s SAR ADC with data-driven noise reduction," in *IEEE ISSCC Dig. Tech. Papers*, Feb. 2013, pp. 270–271.
- [13] V. Giannini, P. Nuzzo, V. Chironi, A. Baschirotto, G. van der Plas, and J. Craninckx, "A 820 μ W 9b 40 MS/s noise-tolerant dynamic-SAR ADC in 90 nm digital CMOS," in *IEEE ISSCC Dig. Tech. Papers*, Feb. 2008, pp. 238–610.
- [14] P. Harpe, Y. Zhang, G. Dolmans, K. Philips, and H. de Groot, "A 7-to-10b 0-to-4 MS/s flexible SAR ADC with 6.5-to-16 fJ/conversion-step," in *IEEE ISSCC Dig. Tech. Papers*, Feb. 2012, pp. 472–474.

- [15] M. Ding, P. Harpe, Y.-H. Liu, B. Busze, K. Philips, and H. de Groot, "A 5.5 fJ/conv-step 6.4 MS/s 13b SAR ADC utilizing a redundancy-facilitated background error-detection-and-correction scheme," in *IEEE ISSCC Dig. Tech. Papers*, Feb. 2015, pp. 1–3.
- [16] C.-C. Liu, S.-J. Chang, G.-Y. Huang, and Y.-Z. Lin, "A 10-bit, 50-MS/s SAR ADC with a monotonic capacitor switching procedure," *IEEE J. Solid-State Circuits*, vol. 45, no. 4, pp. 731–740, Apr. 2010.
- [17] A. V. den Bosch, M. Steyaert, and W. Sansen, "An accurate statistical yield model for CMOS current-steering D/A converters," in *Proc. IEEE Int. Symp. Circuits Syst.*, May 2000, pp. 105–108.
- [18] J. A. Fredenburg and M. P. Flynn, "Statistical analysis of ENOB and yield in binary weighted ADCs and DACs with random element mismatch," *IEEE Trans. Circuits Syst. I, Reg. Papers*, vol. 59, no. 7, pp. 1396–1408, Jul. 2012.
- [19] A. M. Abo and P. R. Gary, "A 1.5-V, 10-bit, 14.3-MS/s CMOS pipeline analog-to-digital converter," *IEEE J. Solid-State Circuits*, vol. 34, no. 5, pp. 599–606, May 1999.
- [20] P. J. A. Harpe *et al.*, "A 26 μ W 8 bit 10 MS/s asynchronous SAR ADC for low energy radios," *IEEE J. Solid-State Circuits*, vol. 46, no. 7, pp. 1585–1595, Jul. 2011.



Ming Ding received the B.E. degree from the Huazhong University of Science and Technology, Wuhan, Hubei, China, in 2009, and the M.Sc. degree from the Eindhoven University of Technology, The Netherlands, in 2011.

In 2011, he joined the Holst Centre/imec, Eindhoven, The Netherlands, as a Researcher. He has been involved in ultralow-power wireless transceivers, with a main focus on ADC and analog baseband circuits research and design.



Pieter Harpe (SM'15) received the M.Sc. and Ph.D. degrees from the Eindhoven University of Technology, The Netherlands.

In 2008, he joined as a Researcher with the Holst Centre/imec, Eindhoven, The Netherlands, where he has been involved in ultralow-power wireless transceivers, with a main focus on ADC research and design. In 2011, he joined the Eindhoven University of Technology as an Assistant Professor on low-power mixed-signal circuits. Since 2012, he has been the co-organizer of the yearly workshop on

Advances in Analog Circuit Design. He currently serves as a Distinguished Lecturer of the IEEE Solid-State Circuits Society.

Dr. Harpe became a Member of the Technical Program Committees of ISSCC and ESSCIRC since 2013.



Yao-Hong Liu (S'04–M'10) received the Ph.D. degree from National Taiwan University, Taipei City, Taiwan, in 2009.

He joined Terax Communication, Taiwan, from 2002 to 2003, where he is involved in RFIC for Bluetooth. From 2003 to 2006, he was with VIA technology, New Taipei City, Taiwan, where he was involved in GSM and WCDMA transceiver products. He joined Mobile Devices, Zhubei City, Taiwan, in 2006, to work on OFDM-based transceivers for WiFi and WiMAX. Since 2010, he has been with the Holst

Centre/imec, Eindhoven, The Netherlands, where he is currently a Principal Scientist. His current research interests include the ultralow power and highly digitally assisted RF transceivers for wireless healthcare and Internet-of-Things applications.

Dr. Liu currently serves as a Technical Program Committee Member of the IEEE RFIC Symposium.



Benjamin Busze received the Dipl.-Ing. degree in electrical engineering and information technology from the RWTH-Aachen University, Aachen, Germany, in 2008.

He is currently a Researcher in Digital Signal Processing and Digital Circuit Design. He joined the Holst Centre/imec in 2008, where he has been involved in digital baseband design for wireless systems.



Kathleen Philips received the Ph.D. degree in electrical engineering from the Eindhoven University of Technology, The Netherlands.

She started her career with Philips Research, The Netherlands, where she is involved in analog and mixed-signal circuits. She joined the Holst Centre/imec in 2007, where she is currently leading a program on ultralow power wireless, processing and sensing systems. This is part of an open innovation collaboration, together with local and international industry. She is currently a Program Director of

Perceptive Systems for the IoT with imec. She has 20 years of experience in the domain of low power mixed-signal, RF, and integrated system design. Her research interests include applications in the area of infrastructure and person-centric IoT systems, with a focus on ultralow power communication and sensing.



Harmke de Groot (M'11) received the M.Sc. degree in electrical and electronics engineering from the Eindhoven University of Technology, The Netherlands, in 1997, and the M.B.A. degree from the TIAS Business School, Tilburg, The Netherlands, in 2013.

She was with NXP, Eindhoven, The Netherlands, Philips Research, and Microsoft, Washington, USA. She was with the Holst Centre/imec, Eindhoven, The Netherlands, in 2008, where she is currently a Senior Director for Perceptive Systems for the

Intuitive Internet of Things. These heterogeneous connected systems use their own sensors as well as information from the cloud to build a view of the world surrounding them and in such a way realize a natural and intuitive experience for the end-user. Her team is internationally recognized for their work in the field of large-scale sensor networks for IoT, high-speed 5G networks, and low power and low cost sensors. Imec contributes to the Internet of Things revolution by developing innovative algorithms, network, radio, dsp and sensor solutions for person-centric IoT, smart cities and buildings, and automotive applications, realizing that the traditional borders between these applications domains are quickly fading. Together with a wide range of industrial and academic partners, this Research and Development Program addresses the challenges of limited autonomy, functionality, interoperability, ease of use, data fusion, and security to enable a wide range of new applications and a truly intuitive user experience. She has co-authored over 80 publications including a book on embedded system design.